IEEE Access
Multidisciplinary | Rapid Review | Open Access Journal

Received 30 April 2024, accepted 26 June 2024, date of publication 17 July 2024, date of current version 29 July 2024.

Digital Object Identifier 10.1109/ACCESS.2024.3430219

RESEARCH ARTICLE

Optical Fiber Bragg Grating-Based Measurement of Fluid-Structure Interaction on a Cantilever Panel in High-Speed Flow

LUKE POLLOCK[1], HARALD KLEINE[1], ANDREW NEELY[1], AND GRAHAM WILD[2], (Member, IEEE)

[1]School of Engineering and Technology, University of New South Wales Canberra (UNSW Canberra), Campbell, ACT 2612, Australia
[2]School of Science, University of New South Wales Canberra (UNSW Canberra), Campbell, ACT 2612, Australia

Corresponding author: Luke Pollock (l.pollock@unsw.edu.au)

This work was supported by the Air Force Office of Scientific Research under Award FA2386-22-1-4081.

ABSTRACT Optical fiber Bragg grating (FBG) technology offers many advantages over conventional electrical sensors for the measurement of fluid-structure interaction (FSI). In this work, FBGs are used to measure the dynamic response of 3 mm, 2 mm, and 1 mm thick aluminum cantilever panels under the influence of Mach 2 reflected shock impingement in the UNSW Canberra supersonic blowdown facility. Results compared during start-up and steady-state with high-speed digital video schlieren and laser Doppler vibrometry indicate that FBGs can successfully capture the temporal and spectral characteristics of high-speed FSI. The torsional mode of the 1 mm plate is spectrally captured by the FBG with only a single sensor. Furthermore, it is shown that error in the FBG signal is comparable to that of a laser Doppler vibrometer. The greatest challenge remains the efficient decoupling of thermal effects.

INDEX TERMS Structural health monitoring (SHM), integrated vehicle health monitoring (IVHM), fiber Bragg grating (FBG), fluid-structural interaction (FSI), fluid-thermal-structural interaction (FTSI), aeroelasticity, aerothermoelasticity, high-speed, supersonic, hypersonic.

I. INTRODUCTION

The extreme environments in which high-speed vehicles (HSVs) and their mass-constrained designs operate, result in high failure rates [1]. Notable cases include DARPA's Falcon HTV-2 that experienced ''unexpected aeroshell degradation'' [2], wind tunnel tests of the X-20, and the North American X-15 where panel flutter resulted in structural damage [3]. A notable cause of HSV failure is from fluid-thermal-structural interaction (FTSI) wherein the complex non-linear fluid and structural physics couple together to introduce new phenomena. FTSI can result in reduced life, diminished aerodynamic, stability, control, and propulsive performance, and in extreme cases, catastrophic failure.

Greater understanding of FTSI has improved HSV designs, yet there remain challenges. There is a scarcity of high-fidelity data with the majority of data being collected from ground-based testing. Hypersonic wind tunnels are typically limited to very short duration flows (typically less than 1 second). The use of supersonic blow-down facilities with longer test times enables representative structures to be observed for longer durations with reduced operating costs and turnaround times, albeit at lower Mach numbers.

An alternative approach to ground testing is through the use of an in-flight monitoring system for measuring FTSI or a ''failure detection system'' as introduced by [4] for hypersonic vehicles. This technology is an attractive means of improving vehicle reliability as it enables quasi-real time monitoring of the state of the vehicle. A conceptual depiction of such a monitoring system is shown in Fig. 1. Monitoring structural distortion during flight demands a departure from the sensing and instrumentation systems typically employed in ground-based testing. Advanced sensing systems become essential as parameters of interest exhibit wide spatial and temporal scales and must be capable of being able to survive the extreme flight environment.

The associate editor coordinating the review of this manuscript and approving it for publication was Ming Xu.

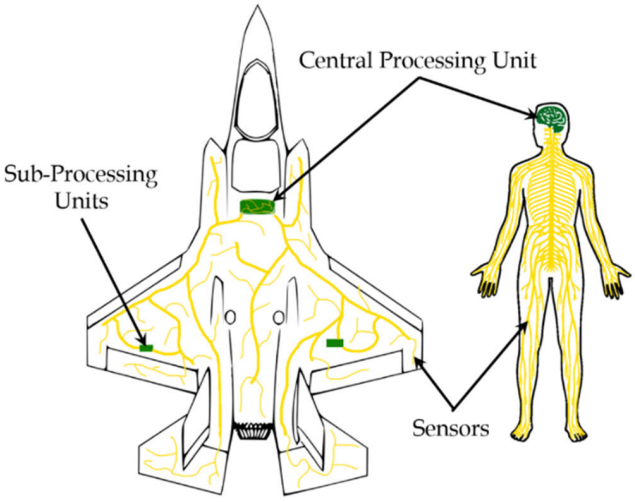

FIGURE 1. General principle of a distributed health monitoring network.

Distributed optical fiber sensing (OFS) systems possess the requisite characteristics for this purpose. While some conventional sensing technologies may be applicable, the immunity to electromagnetic interference, lightweight nature, ability to operate at elevated temperatures, and versatility make optical fibers particularly well-suited for the task. The high multiplexing capabilities of OFS sensors open the door to order-of-magnitude increases in sensor quantities and, consequently, data production and spatial sensing resolution compared to historical HSV programs [5], [6]. The EMI immunity of fiber optic systems also presents the ability for an integrated fly-by-light architecture [7] and realization of shape morphing concepts [8]. The research in this paper is directly applicable to future HSVs, contributing to data acquisition and enhancing understanding of flow physics, along with quasi-real time command and control functionality.

Whilst various OFS technologies exist, including interferometric, scatter, and fiber Bragg gratings (FBGs), FBGs stand out for their ease of multiplexing and exceptional versatility. FBGs have proven effective in sensing and monitoring static strain, temperature, pressure, radiation, corrosion, and dynamic strain, such as vibration, ultrasound, acousto-ultrasonics, and acoustic emissions [9]. Notably, FBGs have demonstrated applicability as temperature sensors in environments reaching up to 1500 K in silica fiber and 2000 K in sapphire fiber [10]. Consequently, FBGs are ideally suited for the development of an integrated distributed sensing network dedicated to the measurement of fluid-thermal-structural interactions (FTSI).

An advantage of FBG sensors is their ability to be multiplexed, where multiple gratings can be inscribed in a single length of fiber. As each grating has a different Bragg wavelength, multiple sensors can be read simultaneously. The Bragg wavelengths must be separated sufficiently to prevent crosstalk over the expected dynamic range of the sensor. Various methods for interrogating multiplexed FBGs exist including time division multiplexing (TDM) and wavelength division multiplexing (WDM). Presently, the utilization of dense ultra-short FBG arrays has showcased unparalleled multiplexing capabilities, with demonstrations achieving over 600 discrete gratings per meter of fiber [5].

In this paper, FBGs are applied to measure the fluid-structure interaction (FSI) of a cantilever panel under the influence of shock impingement in a Mach 2 flow. These ground-based experiments are conducted to qualify the use of FBGs for flight testing and to improve experimental testing capabilities.

Contemporary commercial off the shelf (COTS) FBG interrogator technology delivers typical wavelength resolutions of 1 pm or 5 pm. In the context of the initial sizing for the experiments, a compliant cantilever panel measuring 135 mm x 45 mm (length x width) can be utilized alongside Euler-Bernoulli beam theory to ascertain the deflection sensitivity of the interrogation system. The ensuing analysis, illustrated in Fig. 2, reveals that a coarse interrogator resolution results in tip deflection resolutions of the order of 50 to 5 microns, whilst a finer interrogator resolution extends the capability to measure deflections of the order of 10 to 2 microns. More complex geometries such as fully-clamped panels exhibit higher-order vibrational modes which introduce nodes and antinodes at different locations, necessitating an array of strain sensors for comprehensive measurement [6].

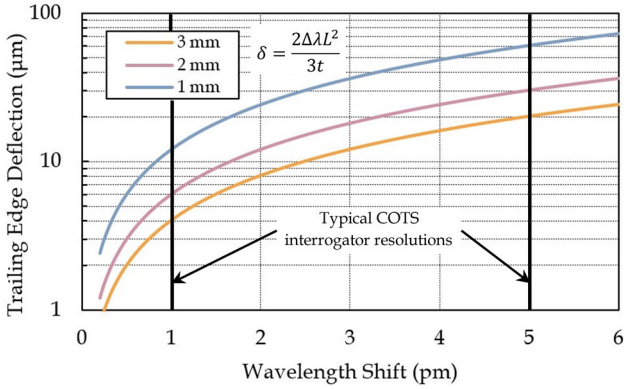

FIGURE 2. Equivalent FBG wavelength shift as a result of trailing edge tip displacement of different plate thicknesses.

A multiplexed array of sensors also permits the ability for shape reconstruction. Shape reconstruction is a method that determines the shape or deflection of a structure from discrete strain measurements [11]. Ko's displacement theory is one such method that is derived from Euler-Bernoulli beam theory. Typically, polynomial fits are created along parallel multiplexed sensor lines, called strain lines (ϵ). These strain lines are then used to solve for the out-of-plane displacement (δ) along the length of the beam (x) using (1) if the beam's thickness (t) is known. Multiple strain lines have been shown to be capable of capturing complex

bending/twisting behavior.

$$\frac{d^2\delta}{dx^2} = \frac{-2}{t}\epsilon\,(x) \tag{1}$$

The aim of this research is to introduce optical fiber sensing technology, in the form of FBGs for the measurement of FSI in high-speed flows. The FBGs will be used to provide strain information in the ground test whilst simultaneously supporting their validation for wider use on flight vehicles. Results are compared with high-speed video schlieren imagery and measurements obtained from laser Doppler vibrometery. The usefulness and challenges in using FBGs are also discussed. A full analysis of the FSI case will be addressed in a follow up article.

II. METHODOLOGY

A. UNSW CANBERRA SUPERSONIC BLOWDOWN TUNNEL

The UNSW supersonic blowdown wind tunnel facility employs three compressed air reservoirs totaling a volume of 30m^3 at a pressure of 14 MPa. Interchangeable nozzle liners permit operation at Mach 2, 2.4, and 3. The settling chamber can be operated between gauge pressures of 100 kPa and 400 kPa and is controlled by a closed loop pneumatic actuator [12]. The tunnel allows for total flow times up to 30 seconds of which approximately 20 seconds is the test flow time as the result of an un-evacuated test section and the resulting transient start-up and shut-down. A layout of the tunnel is obtained from [12] and is shown in Fig. 3.

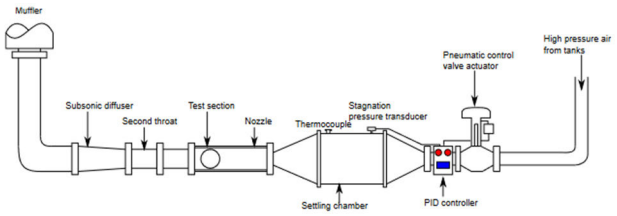

FIGURE 3. General schematic of the supersonic blowdown tunnel [12].

B. DESIGN OF THE REFLECTED SHOCK IMPINGEMENT CASE

Due to the limitations imposed by the blowdown tunnel, the installation of large models is restricted to prevent flow blockage, as described by the Kantrowitz limit [13]. A commonly employed rule of thumb for this facility is to ensure that the projected frontal area of any model remains below 10% of the tunnel cross-section. With a nominal tunnel cross-section measuring 135 mm x 90 mm, this sets a constraint that any model must have a projected frontal area not exceeding 12,000 mm^2. In previous FSI studies either an angle-of-attack [14] or shock generator [15] have been used to create an aerodynamic load. However, the flow blockage limitation in this facility severely restricts the ability to incline the cantilever model or include an additional rigid body. To illustrate this challenge, a relationship between the model's inclination angle and blockage percentage is presented in Fig. 4 below. It becomes evident that the maximum angle of attack that can be employed while staying below the specified threshold is approximately 1.7°. However, such a shallow angle is unlikely to generate the dynamic response necessary for an FSI experiment.

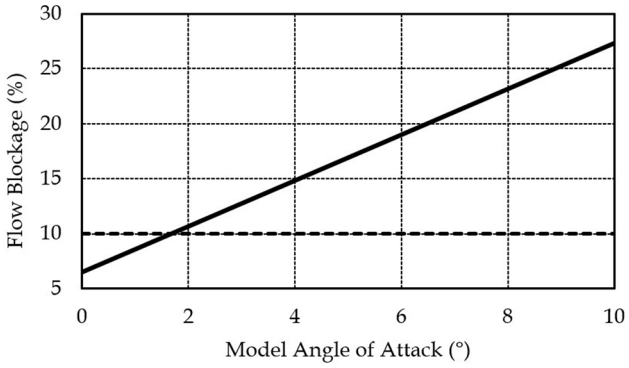

FIGURE 4. Flow blockage of the test section as a function of the model's angle of attack.

In response to this limitation, an alternative approach has been adopted. The leading-edge shock from the model is strategically reflected off the tunnel walls, directing it to impinge upon the cantilever plate, as shown in Fig. 6. This arrangement generates an aerodynamic load that is sufficient to excite the model. Importantly, this alternative setup allows for the examination of FSI in the presence of a shock impingement, providing valuable insights into the system's behavior.

Between the tunnel's sidewalls, a rigid steel forebody, referred to as the ''hammerhead,'' is securely mounted. The hammerhead design was shown by [16] to significantly reduce edge effects and lead to a more two-dimensional flow across the compliant panel. The cantilever panel is adhered to a steel insert, which is then mechanically fastened to the hammerhead. This design facilitates the interchangeability of panels with varying thickness, thereby offering different levels of compliance. Additionally, the model incorporates internal channels for accommodating instrumentation, including the FBGs, strain gauges, thermocouples, pressure gauges, etc.

The leading edge is rigidly constrained on the forebody by a sliding T-slot. This arrangement not only provides the flexibility to alter the leading-edge angle but also allows for adjustments in the model's length. The assembled model, along with its positioning in the wind tunnel, is illustrated in Fig. 5.

An additional design feature takes advantage of the asymmetry in the mounting points on the tunnel walls. This arrangement allows for the asymmetrical reflection of the model to alter the location of shock impingement on the cantilever. In the scenario of a ''panel up'' model, the longer path length is suitable for the Mach 2 flow case. Conversely, a ''panel down'' model, characterized by a shorter path length, is used for the Mach 3 case. A diagram illustrating the

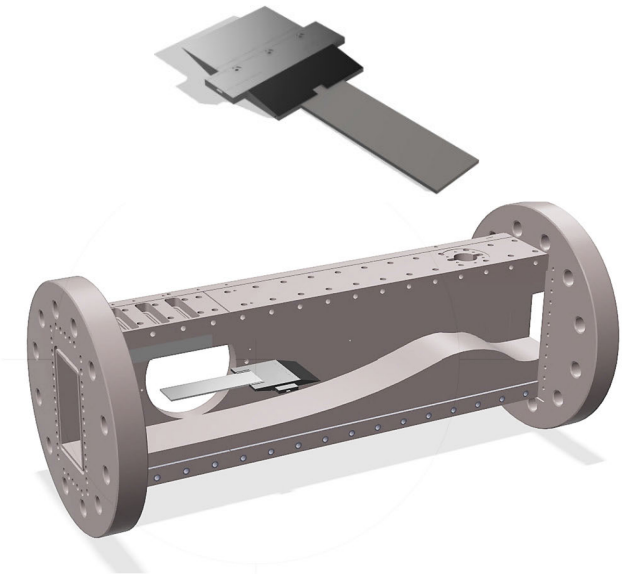

FIGURE 5. Cantilever model (top) and its mounted location in the tunnel (bottom).

Mach 2 and 3 flow cases is presented in Fig. 6 below. The incident shocks on the wall, annotated as S_N, where N is the operating Mach number, result in the formation of an induced separation shock (R_{N1}) and a reattachment shock (R_{N2}) [17]. Thus far, only the Mach 2 testing campaign has been conducted with future testing planned at Mach 3.

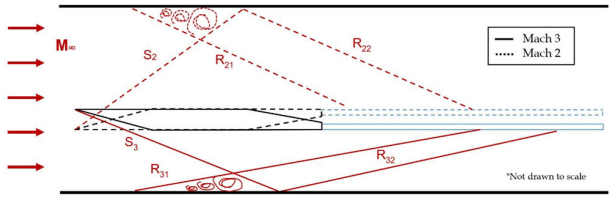

FIGURE 6. Representative schematic of the Mach 2 and Mach 3 flow cases.

The nominal freestream flow properties for both the Mach 2 and Mach 3 cases are provided below in Table 1. Dry air is sourced from the pressure reservoirs at ambient temperature.

TABLE 1. Nominal freestream flow properties for Mach 2 and Mach 3 in the supersonic tunnel.

	Mach 2	Mach 3
Static Pressure (kPa)	25.56	9.528
Static Temperature (K)	166.7	107.1
Velocity (m/s)	517.6	622.3
Unit Reynolds Number (m^{-1})	8.103×10^6	10.72×10^6

To establish the relevance of the current FSI case and draw comparisons with other experimental work, a map of reduced frequency (f_r – Eqn. 2.1) versus the aerodynamic to structural compliance ratio (Λ – Eqn. 2.2) has been established. This map, adapted from [18] and augmented with the inclusion of the current study, serves as a valuable tool for analysis. As Λ increases, the aerodynamic loads from the flow also increase, shifting the response from being structurally dominated towards aerodynamically dominated. Similarly, a higher reduced frequency suggests a less compliant panel. This map, given in Fig. 7, is divided into two distinct regions. Experiments on the right side of the graph are representative of fully clamped scenarios, while those on the left side involve either cantilever or partially clamped configurations. Three experiments are analyzed in this article with an aluminum panel of thicknesses 1 mm, 2 mm, and 3 mm. The planned experiments are strategically positioned to address a gap in the literature at lower reduced frequencies.

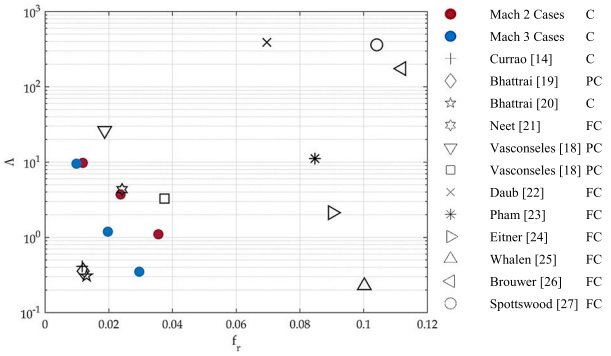

FIGURE 7. Map of reduced frequency and aerodynamic to structural compliance ratio for previous experimental work in FSI. C = Cantilever, FC = Fully Clamped, PC = Partially Clamped.

The equations for f_r and Λ are provided below, where L is the total length of the panel, W is the width, f_s is the first natural frequency in Hertz, u_∞ is the freestream flow velocity, ρ_∞ is the freestream density, E is Young's Modulus, I is the moment of inertia, and M_∞ is the freestream Mach number [18].

$$f_r = \frac{Lf_s}{u_\infty} \tag{2.1}$$

$$\Lambda = \frac{\rho_\infty u_\infty^2 WL^3}{EIM_\infty} \tag{2.2}$$

The natural frequencies of the plates have been calculated using several different methods. Equation (3) provides an analytical method for a cantilever Euler-Bernoulli beam and is compared to solutions obtained from the finite element method employing beam and plate elements.

$$f = \frac{1.875^2}{2\pi}\sqrt{\frac{EI}{\rho AL^4}} \tag{3}$$

Table 2 summarizes the results. All three methods agree well with each other with the plate element solution obtaining slightly higher frequencies as it accounts for in-plane stresses.

The plate element solution is used to obtain the first three modes of all thicknesses in Table 3. Only the plate element can calculate twisting and bending/twisting modes which have been encountered in the experiments.

TABLE 2. First mode frequencies of the plate calculated using three different methods.

	First Mode Analytical Beam (Hz)	First Mode Finite Element Beam (Hz)	First Mode Finite Element Plate (Hz)
1 mm	44.80	44.806	45.844
2 mm	89.61	89.6	91.615
3 mm	142.25	139.96	142.99

TABLE 3. First three modes of the plates as calculated using the finite plate element.

	First Mode (Hz)	Second Mode (Hz)	Third Mode (Hz)
1 mm	45.844	278.23	286.21
2 mm	91.615	551.6	571.58
3 mm	142.99	852.51	890.94

III. INSTRUMENTATION

A. FIBRE BRAGG GRATINGS

Fiber Bragg gratings (FBGs) are spectrally reflective elements embedded in the core of an optical fiber. These gratings are formed by introducing a series of periodic variations in the refractive index of the core, resulting in the creation of a Bragg reflector that acts as a mirror to a specific wavelength [20]. Several methods exist for manufacture, the most common being the inscription of a masked photosensitive optical fiber with an ultraviolet laser. Photosensitive optical fibers are obtained by doping the fiber during manufacturing with the rare earth element Germanium (Ge).

The reflected wavelength, termed the Bragg wavelength (λ_B), correlates with the local strain and temperature. Therefore, monitoring the change in the Bragg wavelength enables the determination of strain and temperature at the grating location. The relationship between the change in the Bragg wavelength and mechanical strain (ϵ) and temperature (T) is described by (4), where the constants k_ϵ and k_T denote the sensitivity of the FBG to each measurand [28].

$$\frac{\Delta\lambda_B}{\lambda_B} = k_\epsilon \epsilon + k_T \Delta T \tag{4}$$

The sensitivity parameters can be determined using (5.1) and (5.2) and depend on the refractive index (n), Pockels coefficients (p_{12}, p_{11}), Poisson's ratio (ν), the coefficient of thermal expansion (α), and the thermoelastic coefficient (ξ) [29].

$$k_\epsilon = 1 - \frac{1}{2}n^2 \left[p_{12} - \nu\left(p_{12} + p_{11}\right)\right] \tag{5.1}$$

$$k_T = \left[1 - \frac{1}{2}n^2\left(p_{11} + 2p_{12}\right)\right]\alpha + \frac{\xi}{n} \tag{5.2}$$

Expected values and uncertainties for these parameters are obtained from [30] and [31] for a silica optical fiber and are listed in Table 4. Where values could not be obtained an uncertainty of 5% of the expected value has been used.

TABLE 4. Expected properties of a silica optical fiber and their uncertainties.

Parameter	Expected Value (ND)	Uncertainty (±)
ν	0.154	0.018
p_{11}	0.113	0.005
p_{12}	0.252	0.005
n	1.458	0.0729
α	5×10^{-7}	2.5×10^{-8}
ξ	1×10^{-5}	5×10^{-7}

The resulting thermal and mechanical sensitivities are given below in Table 5 where the uncertainties are determined via the method of propagation of uncertainties.

TABLE 5. Calculated FBG sensitivities and their uncertainties.

Thermal Sensitivity (K^{-1})	Mechanical Sensitivity (mm/mm)
$(70.308 \pm 5.426) \times 10^{-7}$	$(7.919 \pm 0.518) \times 10^{-1}$

In these experiments, a single FBG has been affixed to the root of the cantilever plate running parallel to its length using aluminum tape as shown in Fig. 8.

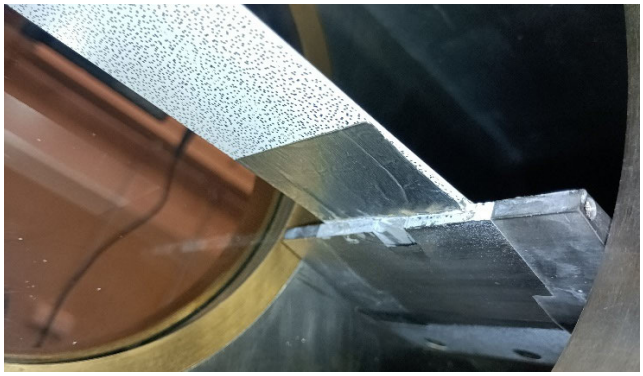

FIGURE 8. An image of the experimental model in the test section with an FBG adhered at the panel root using aluminum tape.

The fiber was routed out through the tunnel wall and was interrogated using a COTS FS22 BraggMETER connected to a laptop via an ethernet interface. The FS22 employs a continuously swept scanning laser and is capable of measuring hundreds of sensors over up to eight channels. Data was acquired at a sample rate of 1,000 samples per second and maximum resolution of 1 pm.

B. SCHLIEREN

Schlieren imagery was obtained using a Z-type configuration [32] with two spherical mirrors of 2.62 m focal length and diameters of 240 mm. A horizontal knife edge was used which allows for the detection of density gradients perpendicular to the direction of the flow. A diagram of the schlieren setup is shown in Fig. 9.

The camera used was a Fastcam Mini AX 200 which is capable of capturing 6,000 frames per second (fps) at a full

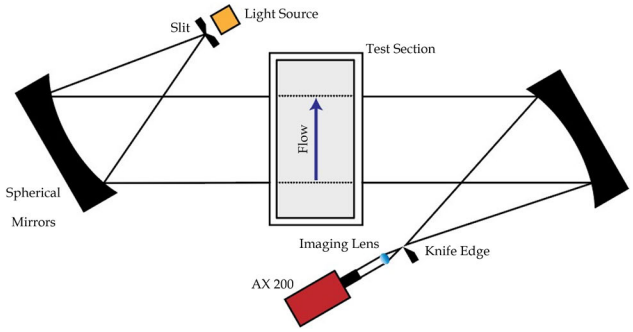

FIGURE 9. Diagram of the Z-type schlieren configuration used in the experiment.

resolution of 1024 × 1024 pixels or up to 900,000 fps with a minimum exposure time of 260 ns. Each experiment was performed at the full resolution and acquired at a rate of 2,500 frames per second with an exposure time of 0.2 ms. Images were then exported in TIFF format after each run for further analysis.

C. LASER DOPPLER VIBROMETER

In addition to the schlieren setup, a Polytec PDV-100 portable laser Doppler vibrometer (LDV) was used to acquire a point velocity at the trailing edge of the plate. Data was sampled at a rate of 20,000 samples per second with an output of 125 mm/s/V and peak-to-peak range of 500 mm/s. The LDV was connected to the tunnel's data acquisition system via BNC interface. An LDV is an interferometric non-contact device typically used for vibrational measurements. The laser is directed at the surface of the structure and the reflected beam acquired allows for the velocity of the structure to be determined from the Doppler shift. LDVs offer exceptional sensitivity and accuracy and unlike accelerometers, do not create a mass load on the structure. The main challenge with the use of an LDV is suitable optical access and alignment of the laser. COTS LDVs can also be prohibitive due to their cost. Unfortunately, the dynamic range of the PDV-100 was not large enough to capture the high velocities of the 1 mm plate, resulting in signal saturation. However, good results were obtained for both the 3 mm and 2 mm cases. Future work aims to upgrade the LDV infrastructure for these more demanding cases.

IV. RESULTS AND ANALYSIS

A. SCHLIEREN IMAGE PROCESSING

Schlieren images were used to track the motion of the plates using an edge finding algorithm. Initially, a gradient-based approach was adopted using the Sobel method [33], [34] to ascertain the edge of the plate. This method proved noisy and challenging and was quickly abandoned. Instead, a binarized approach [35] was adopted where pixels were set based on an intensity threshold. An advantage of this approach was that the threshold could be set to either mask the flow or structural features of the image. Examples are shown in Fig. 10 and Fig. 11. In Fig. 10, a dark mask has been applied to highlight the flow features. Conversely, in Fig. 11, a bright mask removes the flow features and leaves the plate.

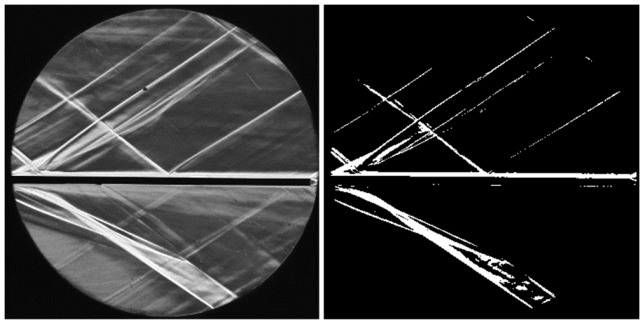

FIGURE 10. Dark masking of the schlieren image to highlight dominant flow features.

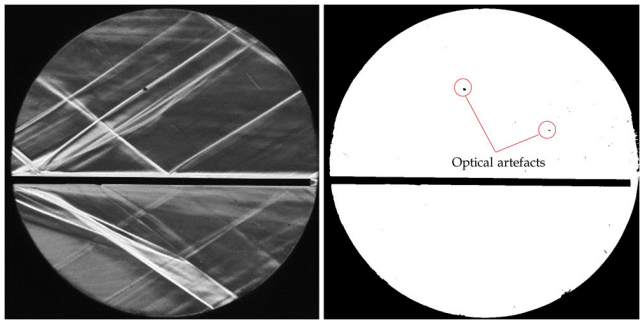

FIGURE 11. Bright masking of the schlieren image to remove the flow features and highlight the plate.

Different threshold values produced varied results and as such, a parametric approach was adopted. Firstly, a schlieren streak diagram [36] was extracted for a certain column of pixels at or near the trailing edge of the plate. An example of this is shown in Fig. 12.

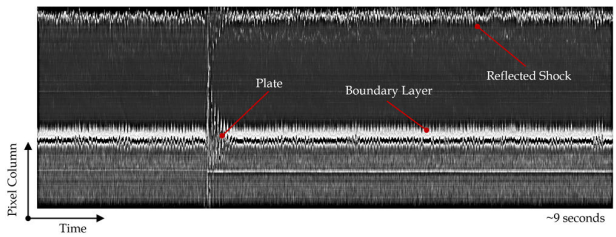

FIGURE 12. Schlieren streak diagram extracted over an experimental run for the 3 mm plate at the trailing edge.

The streak diagram was then binarized using the previously mentioned approach. The threshold was swept over a range of values to obtain several estimates of the plate's edge location, following which the median result was taken. This method, summarized in the flow chart in Fig. 13, proved robust and did not rely on a single user-defined threshold that could bias the analysis.

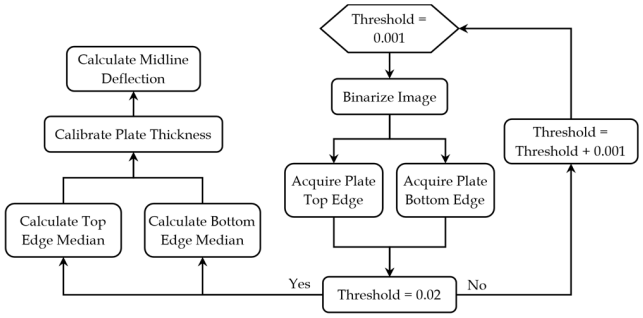

FIGURE 13. Overview of the binarizing method to extract the deflection of the plate from the schlieren images.

Using the binarized method, the positions of both the top and bottom edges of the plate were determined. The thickness of the plate in pixels could then be calculated and converted to its true value. It was observed that the optically determined thickness of the plate varied throughout the experiment due to twisting. As such, the average thickness over the first 100 frames (40 ms) prior to start-up was used to calibrate the results.

The midline location of the plate was then calculated as the average of the top and bottom edge. The resulting displacement is a digital value and can hence show seemingly erroneous jumps in the data. Smoothing could be applied, but this was not done as it removes high frequency components which may prove valuable in analysis. Figure 14 shows an example of the results using the described methodology for the 3 mm plate case. The displacement history is broken into three main regions – pre-start, start-up, and steady-state. A shut-down region also exists at the end of the experiment, similar in feature to the start-up, but was not captured due to the limited acquisition time. The blowdown facility does not feature an evacuated test section and as a result, the start-up process is highly transient.

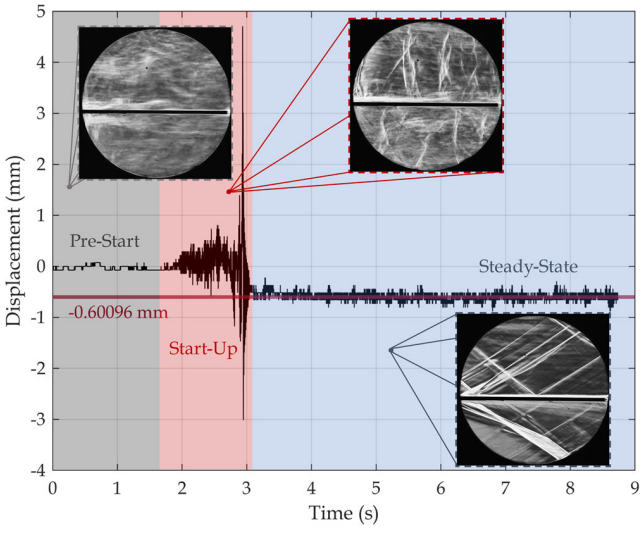

FIGURE 14. Trailing edge displacement of the 3 mm plate extracted from the schlieren images.

The transient start-up has been included in the analysis of the FSI case as it proves to introduce interesting phenomena. Like an impulse, this period of the test creates a broadband excitation in the plate. The spectral characteristics of the experiment have been analyzed using a fast Fourier transformation (FFT) and continuous wavelet transformation (CWT) using the analytic Morse wavelet. The CWT yields a scalogram [37], as shown in Fig. 15, and highlights the presence of the broadband excitation from the start-up. A FFT of the entire displacement history is also shown in Fig. 15. The spectrum is visibly noisy and has been smoothed post-transformation using both a 7th order Savitzky-Golay and moving median filter. The full spectrum is not particularly useful for analysis as the scalogram demonstrates that there are two distinct regions of spectral behavior – the start-up and steady-state. A thorough analysis of this behavior will be undertaken in a separate article with a cursory analysis used here for comparison with the FBG results.

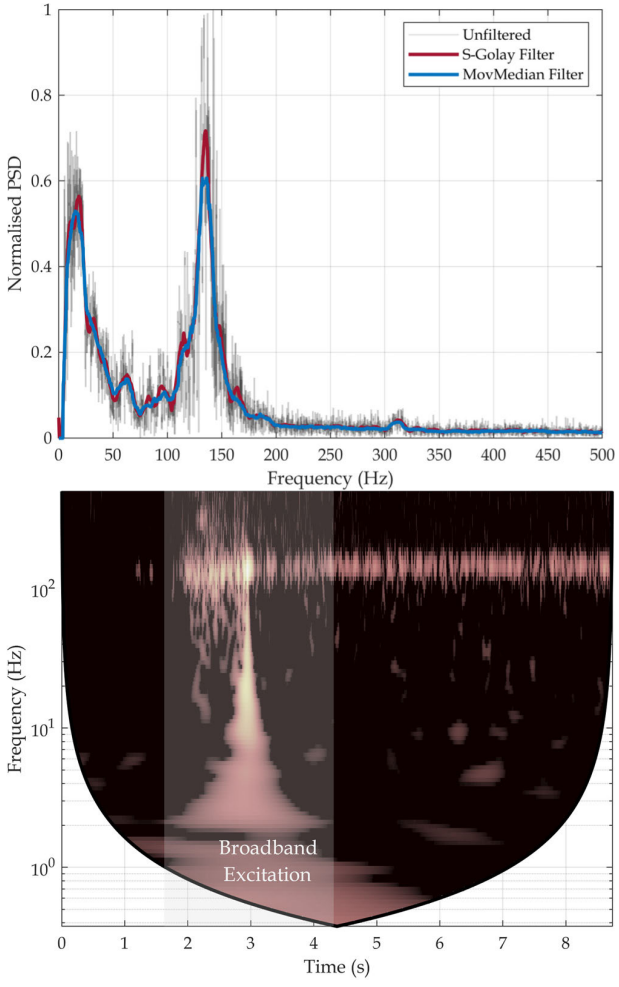

FIGURE 15. Full spectrum of the 3 mm plate (top) and scalogram of the 3 mm plate (bottom).

The FFTs of the start-up and steady-state regions are shown in Fig. 16. The distinct behavior of the two regions is evident with different peak frequency components.

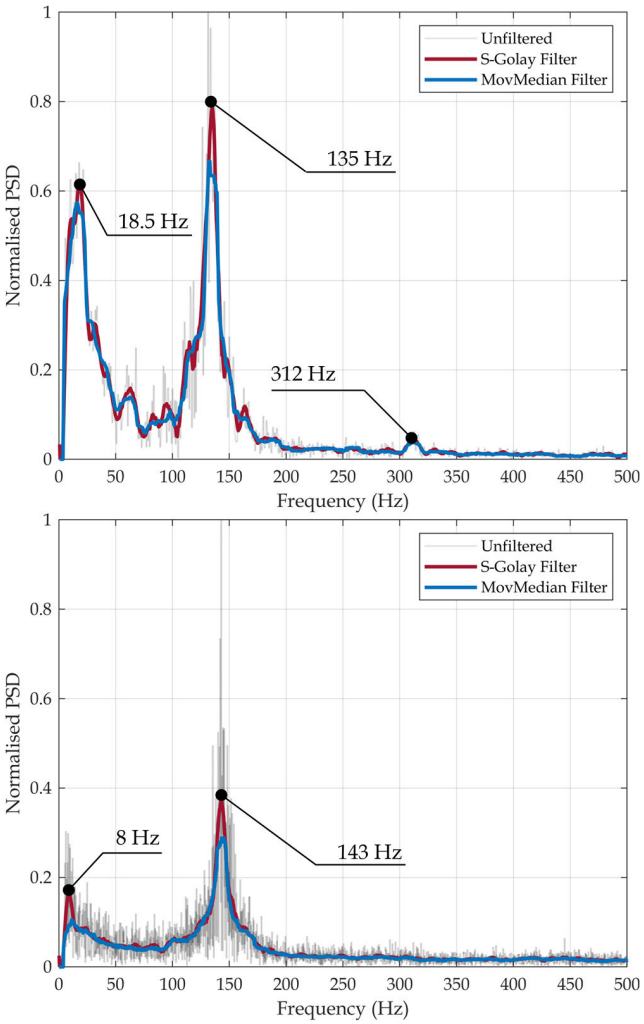

FIGURE 16. Spectra of the start-up region (top) and steady-state region (bottom) for the 3 mm plate obtained from schlieren imagery.

Likewise, the start-up region demonstrates broader spectral content, including stronger low frequency components.

A summary of the dominant frequency component in the start-up and steady-state regions is shown in Table 6. The steady-state deflections are also shown as well as the computed first mode frequencies from the finite plate elements. The 1 mm case shows significant aerodynamic stiffening and geometric non-linearities due to large deflections which result in an increased frequency.

TABLE 6. Summary of the features extracted from the schlieren imagery.

	Steady-State Deflection (mm)	FEA Natural Frequency (Hz)	Start-Up Frequency (Hz)	Steady-State Frequency (Hz)
1 mm	-8.4260	45.844	61.6	137.11
2 mm	-0.91849	91.615	98.6	111
3 mm	-0.60096	142.99	135	143

Of particular note is the 1 mm plate case, which demonstrates strong FSI. A FFT of the steady-state region is shown in Fig. 17. Here it is evident that two modes exist after start-up.

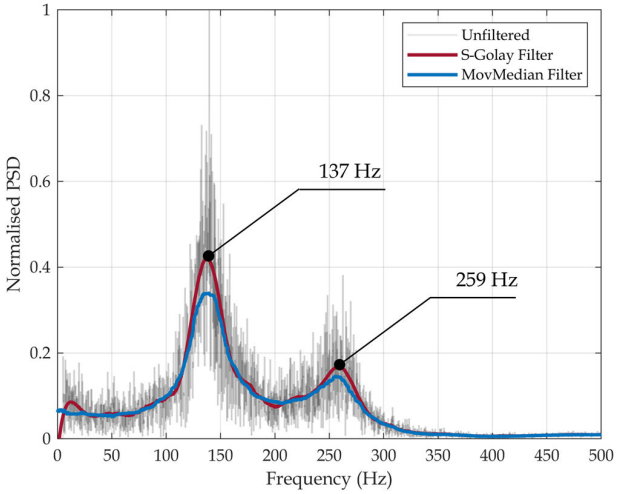

FIGURE 17. Spectra of the steady-state region for the 1 mm plate showing two modes.

The scalogram of the experiment is shown in Fig. 18. Once again, we observe broadband excitation from the transient start-up, however, two distinct frequencies persist into the steady-state region.

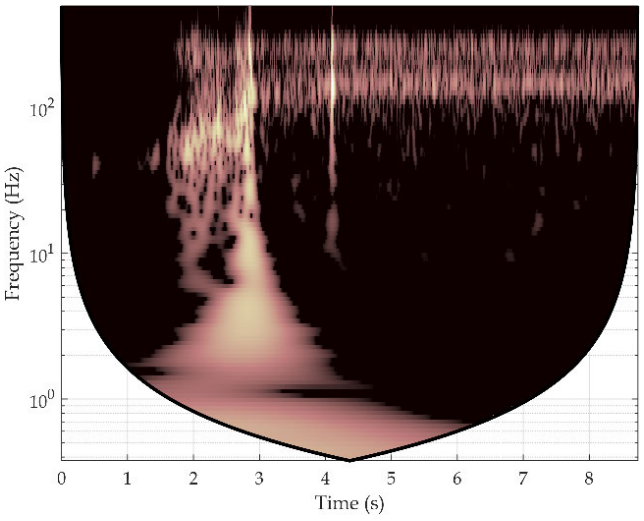

FIGURE 18. Scalogram of the full trailing edge displacement of the 1 mm plate showing the presence of the two modes.

An additional piece of analysis used for validation is a phase portrait [38], shown in Fig. 19 for the 3 mm case. The phase portrait provides a depiction of the velocity at a point on the panel as a function of its displacement. A phase portrait is a useful tool for studying dynamic systems and yields a representation of the orbits in the phase plane. The portrait has been colored in time to show temporal development. For the 3 mm case, a chaotic start-up process is observed followed by the

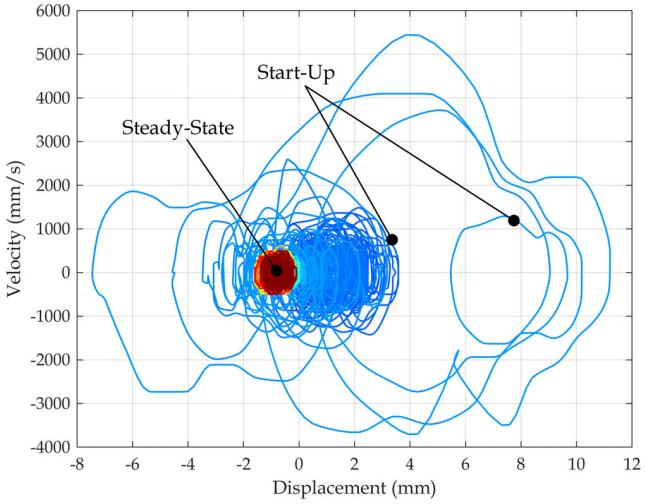

FIGURE 19. Phase portrait for the 3 mm plate showing the chaotic start-up and cyclic attractor in the steady-state region.

presence of a cyclic attractor in the steady-state. The chaotic start-up generates an impulse response in the panel due to the sudden and large aerodynamic load, thereby exhibiting highly non-linear and unsteady behavior. This behavior creates large strains which may result in plastic deformation or sudden failure. The steady-state region is dominated by a steady and stable response, which is more likely to lead to fatigue after long periods of time.

A similar diagram is shown in Fig. 20 for the 1 mm plate but has been colorized by region. The pre-start region, depicted in green, is present at the origin of the diagram. The start-up shows a chaotic repellor, following which the system settles into limit cycle oscillations. As supported by Fig. 18, there is no discernible decrease in oscillation amplitude.

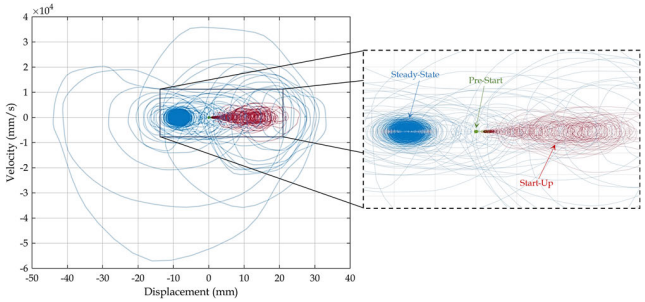

FIGURE 20. Phase portrait for the 1 mm plate, showing the three distinct regions of behavior.

B. LASER DOPPLER VIBROMETRY

In addition to image tracking, the LDV provides another source of data for comparison and validation. The LDV functions as a voltage signal from which the output is transformed into velocity. A FFT of the LDV signals in Fig. 21 show similar noise in the spectra of the plate's vibration. Start-up and steady-state frequencies are extracted and compiled in Fig. 21 and Table 7.

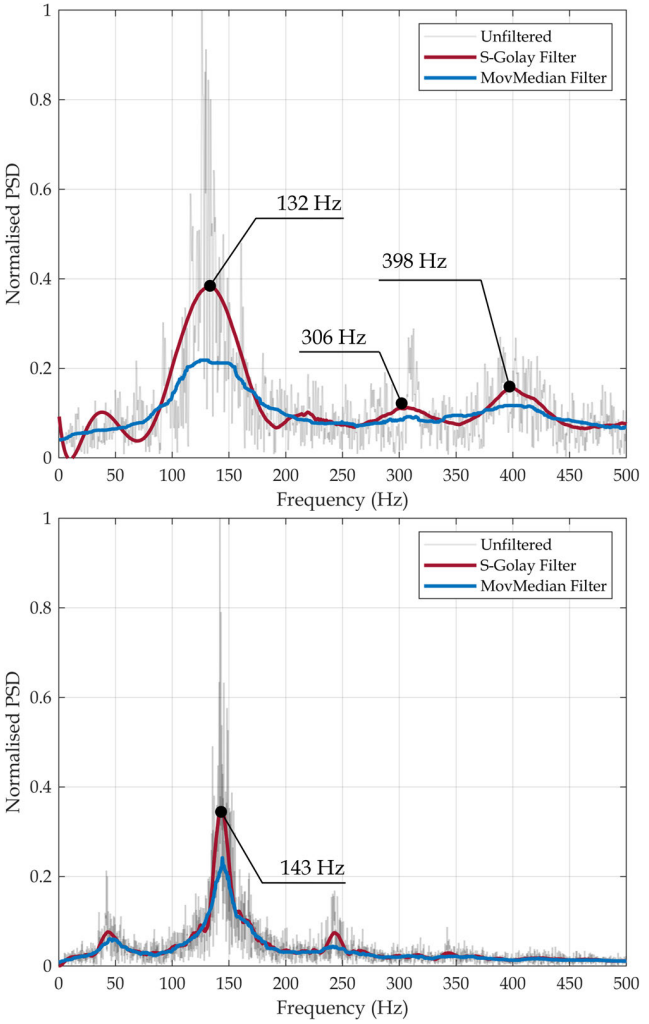

FIGURE 21. Spectra of the start-up region (top) and steady-state (bottom) for the 3 mm plate obtained from the laser Doppler vibrometer.

TABLE 7. Summary of frequencies extracted from the laser Doppler vibrometer results.

	Start-Up Frequency (Hz)	Steady-State Frequency (Hz)
1 mm	NA	NA
2 mm	89	112
3 mm	132	143

C. THERMAL DECOUPLING OF FBGs

A simultaneous advantage and challenge of using FBGs is their sensitivity to both strain and temperature. A standard blow-down tunnel without heated reservoir always generates a fast but cold flow, see the data in Table 1. This means that any model in such a test facility always experiences strain and temperature effects simultaneously, and both effects can be of comparable magnitude.

Many methods exist to decouple the measurands which vary in complexity. In this case, the dynamic nature of the FSI case has been leveraged to create a simple decoupling method. A high pass filter is applied to the signal to remove

low frequency components. These low frequencies result from static deflections and changes in temperature [39]. The resulting high-frequency signal yields the dynamics of the plate. Figure 22 shows the raw signal and decoupled components after applying a 5 Hz high pass filter. A disadvantage of this approach is that the static deflection component observed in the steady-state region is collated and subsequently removed with the thermal signal.

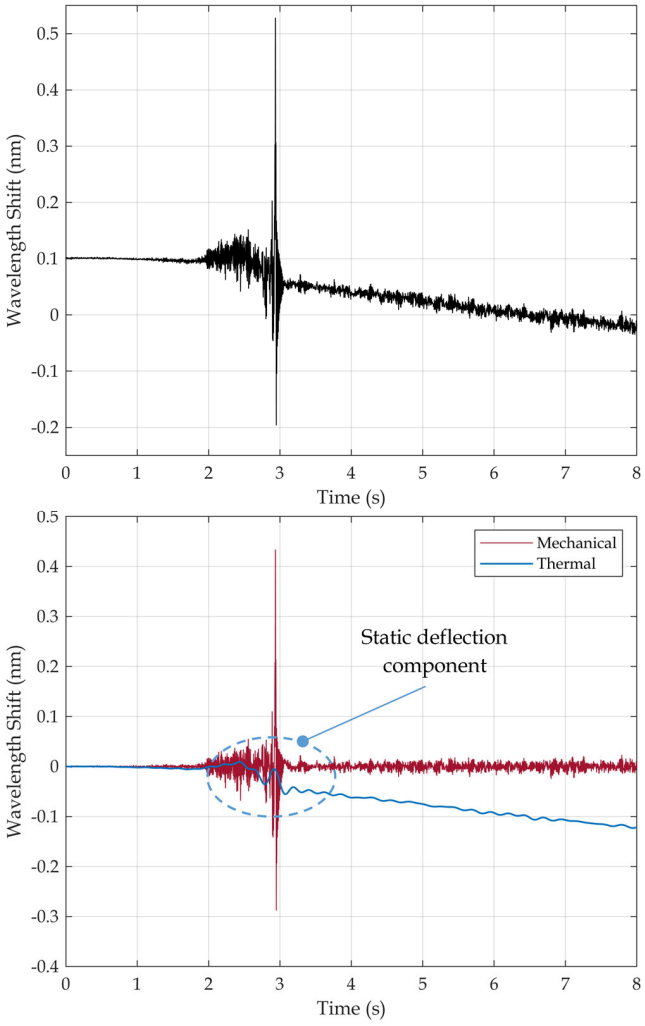

FIGURE 22. Full signal acquired from interrogation of the FBG (top) and the de-coupled dynamic strain and thermal components using a 5 Hz high pass filter (bottom).

Different cut-off frequencies can be applied in an effort to preserve more of the static deflection, but this results in erroneous oscillations. Figure 23 shows a comparison of the decoupled signals using 5 Hz, 1 Hz, and 0.2 Hz cut-off frequencies, respectively. To capture the static deflection of the plate, a more robust decoupling methodology should be used. Several different methods are discussed later in this paper and are planned for future experiments.

The thermal signal can then be converted from a wavelength shift to a temperature change using the sensitivities calculated in Table 5. A zero-wavelength temperature of

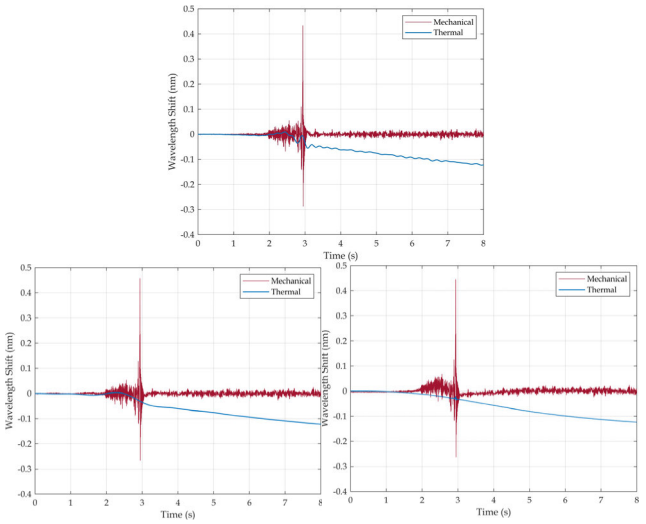

FIGURE 23. Comparison of the de-coupled FBG components using 5 Hz (top), 1 Hz (left), and 0.1 Hz (right) high pass filters.

16°C is added to the signal to account for the initial (room) temperature. To provide a means of comparison, the adiabatic wall temperature (T_{aw}) can be estimated using the recovery factor (r), which is assumed equal to the square root of the flow's Prandtl number (Pr) [40]. The adiabatic wall temperature can then be calculated knowing the absolute temperature of the flow (T_0) and the temperature at the edge of the boundary layer (T_e). In this case, the temperature at the edge of the boundary layer is assumed to be the freestream static temperature behind the leading edge shock.

$$r = \frac{T_{aw} - T_e}{T_0 - T_e} = \sqrt{Pr} \tag{6.1}$$

$$T_{aw} = r\,(T_0 - T_e) + T_e \tag{6.2}$$

The resulting calculations yield a recovery factor of 0.845 and adiabatic wall temperature of 270 K. Figure 24

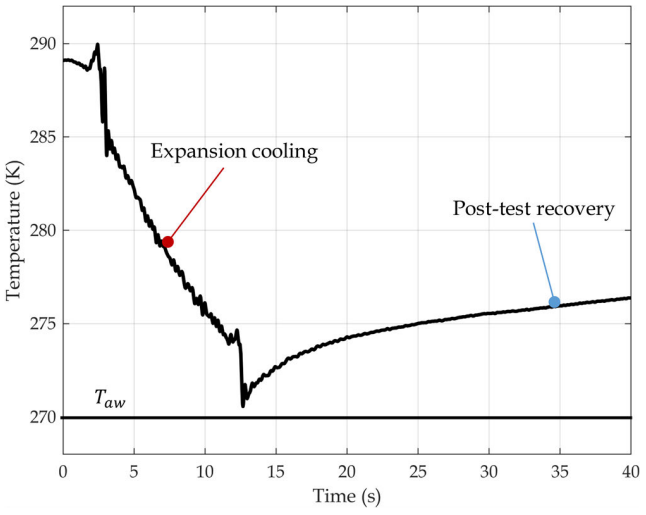

FIGURE 24. Estimated temperature of the FBG during the 3 mm experiment, including post-test temperature recovery.

shows a plot of the low frequency components converted into a temperature with the calculated adiabatic wall temperature indicated. This temperature can only be taken as an estimate of the true value, as it also contains the static deflection component of the signal. Nonetheless, this simple analysis showcases how the FBG can be used simultaneously as a strain and temperature sensor. Further discussion is provided in the proceeding section.

An additional analysis is formed via phase portraits. Figure 25 (top) shows a phase portrait of the entire FBG signal whilst Fig. 25 (bottom) is a phase portrait of only the extracted high-frequency components. The phase portraits of the high-frequency components oscillate around a cyclic attractor located at the origin. The phase portrait of the entire signal shows the potential presence of two attractors and translation between them as a result of start-up. This also demonstrates that our simple method for decoupling the dynamic strain destroys information that would otherwise be valuable for analysis.

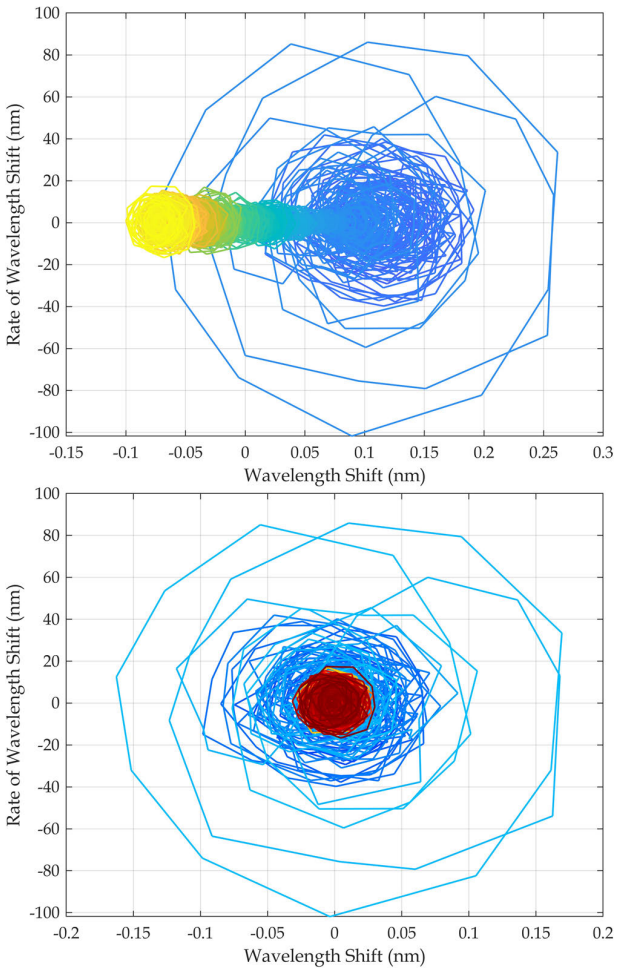

FIGURE 25. Phase portraits for the 3 mm plate using the full FBG signal (top) and the de-coupled dynamic strain using a 5 Hz high pass filter (bottom).

D. FBG COMPARISON

Despite the disadvantages of the simple decoupling method, the dynamic strain can still be analyzed and compared against results obtained from the schlieren and LDV, primarily in the form of a frequency comparison. Firstly, as shown in Fig. 26, the two FFTs are obtained from the start-up and steady-state regions for the 3 mm plate. The results showcase very similar spectral signals, including the first mode frequency. Additional frequencies are observed in the lower end of the spectrum (∼15 Hz) and the higher end (∼315 Hz) during the start-up. A shift in first mode is observed under steady-state that matches the schlieren and LDV analysis.

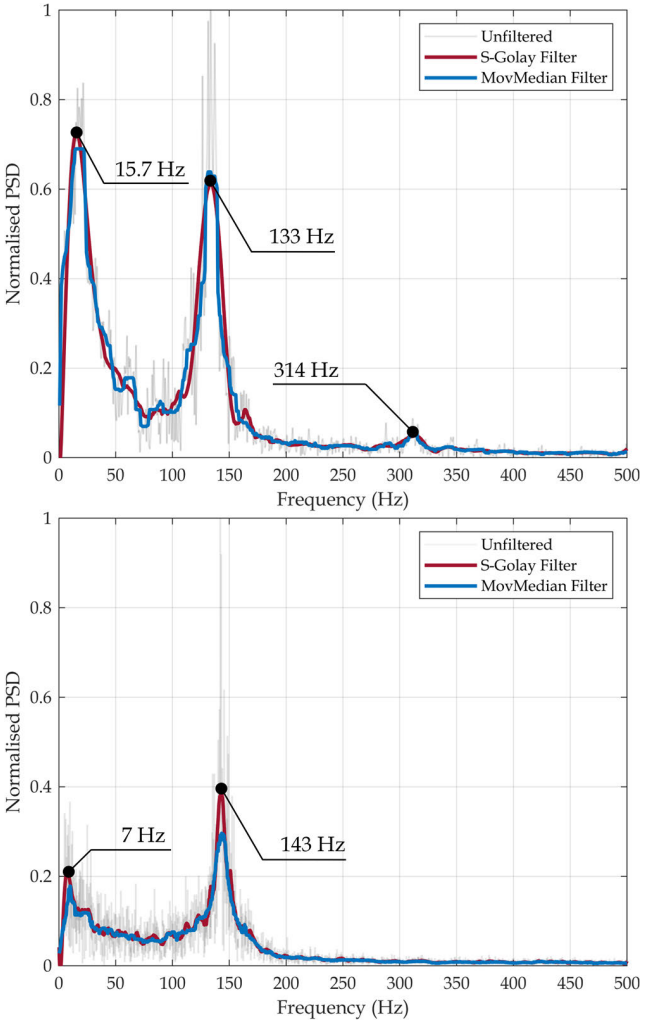

FIGURE 26. Spectra of the start-up region (top) and steady-state region (bottom) for the 3 mm plate obtained from the de-coupled FBG dynamic strain.

An additional comparison is given for the 1 mm plate in the steady-state region. Figure 27 shows results previously presented from the schlieren analysis and the addition of the FFT of the FBG dynamic strain. Firstly, it is noteworthy that the FBG has captured both modes of oscillation. Secondly, the frequencies match very well for both modes. The FBG appears to demonstrate greater levels of spectral noise which

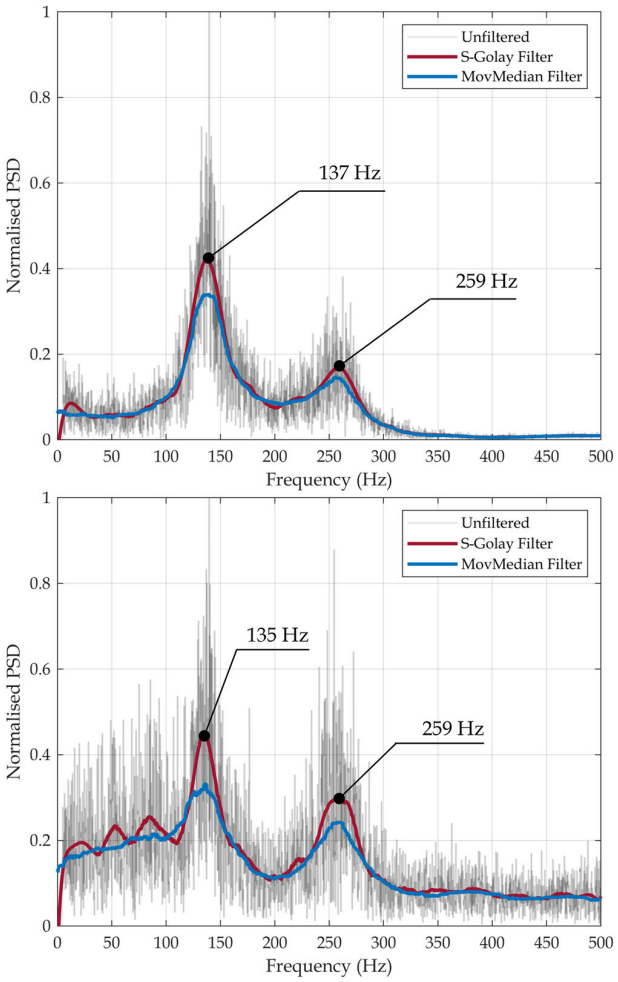

FIGURE 27. Comparison of steady-state spectra for the 1 mm plate obtained from schlieren imagery (top) and the de-coupled FBG dynamic strain (bottom).

is attributed to the method of affixing the sensor to the structure. It is believed that under the large deflections and velocities of the plate, the tape has inefficiently transferred the strain to the sensor. Bonding of the FBG should provide better signal-to-noise ratios.

The frequencies extracted from the FBG dynamic strain signals are compiled in Table 8.

TABLE 8. Summary of frequencies extracted from the de-coupled FBG dynamic strain.

	Start-Up Frequency (Hz)	Steady-State Frequency (Hz)
1 mm	61.1	135.4
2 mm	90.3	109.9
3 mm	133	143

V. DISCUSSION

The results and analysis presented thus far have concluded that optical fiber Bragg gratings are suitable instrumentation for the simultaneous measurement of strain and temperature in a high-speed flow. As a summary, and the main point of comparison, Fig. 28 highlights the dominant frequencies encountered in the start-up and steady-state regions in comparison to the first mode frequencies obtained from the finite plate element method. This summary showcases how FSI becomes more dominant with greater panel compliance as a result of aerodynamic stiffening and geometric non-linearities. The 1 mm panel exhibits very interesting characteristics that will be explored in future work.

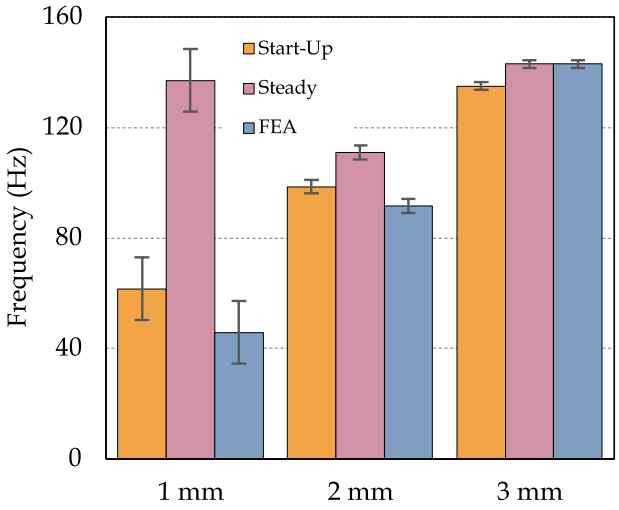

FIGURE 28. Summary of frequencies in the start-up and steady-state regions for all plates, obtained from schlieren imagery.

Figure 29 similarly highlights the frequencies obtained from each of the three methods presented – schlieren, laser Doppler vibrometery, and optical fiber Bragg gratings. Data obtained from the LDV is not available for the 1 mm plate due to signal saturation from large trailing edge velocities. In any case, all methods show very similar results for both the start-up and steady-state regions with the exception of the schlieren analysis of the 2 mm plate in start-up. The discrepancy here is likely a result of the image processing method. These charts illustrate the capability of FBGs to measure FSI induced vibrations in a high-speed flow. Frequencies obtained from FBG and schlieren data agree within 3.5% and 0.75% on average for the start-up and steady-state regions, respectively.

The most challenging aspect encountered was the thermal de-coupling of the FBG signal. In this work, a simple high pass filter approach was adopted to obtain the dynamic strain for analysis. This yielded an aggregate static strain and temperature signal which could only be used to estimate the temperature of the sensor. Typically, a second strain-isolated FBG or temperature sensor is used in conjunction with the strain sensing FBG to decouple the results [41], [42]. Integration of a strain-isolated FBG is not always possible, particularly in environments with strong temperature gradients or small volumes, such as ground test models.

Many other methods exist to de-couple the FBG signal which do not rely on a transducer, several of which

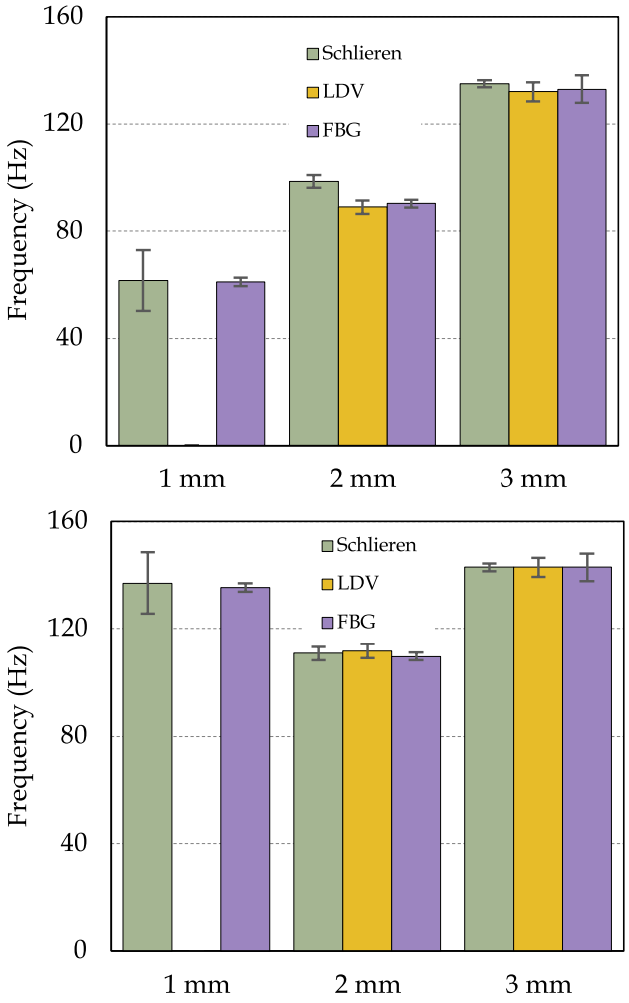

FIGURE 29. Comparison of frequencies obtained using all three methods for the start-up (top) and steady-state regions (bottom).

are discussed here. In [43] a method was examined that enabled simultaneous temperature and curvature sensing and employed a seven-core optical fiber. At the same location along the fiber, FBGs were inscribed in each of the cores, such that curvature could be measured by examining the difference in fiber pairs. Likewise, when curvature and temperature were simultaneously changed, the central core of the fiber was insensitive to the curvature change and hence, could be used to calculate temperature. Others have employed a simple method where a FBG under bending in a non-linear strain region exhibited creation of periodic chirp [44]. Conversely, changes in temperature would generate a uniform change in the Bragg wavelength. An approach where a short-length FBG inscribed into a polarization-maintaining fiber produced two Bragg wavelengths from birefringence has also been applied [45]. The two wavelengths emanate from the slight difference in refractive indices between the two orthogonal polarization modes. The Nelder-Mead simplex algorithm was used to calculate the temperature and strain owing to the different sensitivities of each Bragg wavelength. Finally, [46] used a single phase-shifted FBG to simultaneously measure temperature and strain. The phase shift showed different behavior from temperature and strain, allowing for the two properties to be measured.

All the methods vary in their complexity and interrogation. For example, the measurement of the entire FBG reflected spectra limits the sampling rate of the system. Modern optical spectrum analyzers (OSA) have sampling rates on the order of 1 kHz which can be suitable for low-frequency FSI cases. Alternatively, swept laser approaches with Fourier domain mode locking (FDML) have achieved sweep times of up to 50 kHz which is suitable for virtually all FSI analysis [47].

VI. CONCLUSION

This work has studied the FSI of a Mach 2 reflected shock impingement upon a cantilever panel and the use of fiber Bragg gratings for the measurement of the structural response. The FBG results have been compared with data obtained using digital image processing of high-speed video schlieren as well as velocity measurements obtained from a laser Doppler vibrometer. The results indicate that FBGs can accurately measure the strain on the panel undergoing FSI. Frequencies obtained from FBGs agree within 3.5% and 0.75% with the schlieren results for the start-up and steady-state regions, respectively. The largest challenge encountered was the thermal decoupling of the FBG signal. Here, a simple approach has been adopted wherein a high pass filter was used to extract the dynamic strain for further analysis. Several methods for improving the decoupling and the interrogation of the fiber were discussed and are planned for future experiments. Ultimately, the use of FBGs has been validated for high-speed FSI experiments and highlights the merits of optical fiber systems for both the ground and flight test of high-speed vehicles.

ACKNOWLEDGMENT

Any opinion, finding, and conclusion or recommendations expressed in this material are those of the authors and do not necessarily reflect the views of the United States Air Force. Numerical resources were provided by the National Computational Infrastructure (NCI), under the National Computational Merit Allocation Scheme (NCMAS), which is supported by the Australian Government.

REFERENCES

[1] L. Pollock and G. Wild, "An initial review of hypersonic vehicle accidents," in *Proc. 19th Austral. Int. Aerosp. Congr.*, 2021, pp. 111–116.
[2] Y. Guo, L. Zeng, H. Zhang, G. Dai, A. Wang, B. Qiu, S. Zhou, and X. Liu, "Investigation on aerothermodynamic environment and ablation which lead to HTV-2 second flight test failing," *Acta Aerodynamica Sinica*, vol. 35, no. 4, pp. 496–503, 2017, doi: 10.7638/kqdlxxb-2016.0114.
[3] E. Dowell, "Panel flutter, NASA space vehicle design criteria," NASA, Washington, DC, USA, Tech. Rep. SP-8004, 1970.
[4] F. S. Kirkham and J. L. Hunt, "Hypersonic transport technology," *Acta Astronautica*, vol. 4, nos. 1–2, pp. 181–199, Jan. 1977, doi: 10.1016/0094-5765(77)90040-6.
[5] X. Gui, Z. Li, X. Fu, C. Wang, Y. Wang, H. Li, and H. Wang, "High-density distributed crack tip sensing system using dense ultra-short FBG sensors," *Sensors*, vol. 19, no. 7, p. 1702, Apr. 2019. https://www.mdpi.com/1424-8220/19/7/1702.

[6] L. P. McQuellin, A. Neely, and G. Currao, "Considerations for a hypersonic flight test investigating fluid-thermal-structural interactions," presented at the *Proc. 23rd AIAA Int. Space Planes Hypersonic Syst. Technol. Conf.*, Montreal, QC, Canada, Mar. 2020, doi: 10.2514/6.2020-2419.

[7] G. Wild, "Novel photonics sensing and systems for military metrology," in *Proc. IEEE Metrol. Aerosp. (MetroAeroSpace)*, Jun. 2015, pp. 129–134, doi: 10.1109/METROAEROSPACE.2015.7180640.

[8] A. A. Phoenix, J. R. Maxwell, and G. B. Goodwin, "Morphing high-temperature surfaces for shapeable hypersonic waverider vehicles," presented at the *Proc. Model., Simul. Control Adapt. Syst. Integr. Syst. Design Implement., Structural Health Monitor.*, Snowbird, UT, USA, Sep. 2017, doi: 10.1115/smasis2017-3766.

[9] G. Wild, "Optical fiber Bragg grating sensors applied to gas turbine engine instrumentation and monitoring," presented at the *IEEE Sensors Appl. Symp. Proc.*, Galveston, TX, USA, Feb. 2013. [Online]. Available: https://ieeexplore.ieee.org/abstract/document/6493583

[10] C. R. Liao and D. N. Wang, "Review of femtosecond laser fabricated fiber Bragg gratings for high temperature sensing," *Photonic Sensors*, vol. 3, no. 2, pp. 97–101, Jun. 2013, doi: 10.1007/s13320-012-0060-9.

[11] L. Pollock and G. Wild, "Data-driven shape sensing of a hypersonic inlet ramp," *engarXiv*, 2024, doi: 10.31224/3817.

[12] V. Sridhar, "Computational and experimental investigation of supersonic two-dimensional and axi-symmetric shallow open cavities," M.S. thesis, UNSW, Sydney, NSW, Australia, 2014, doi: 10.26190/unsworks/17153.

[13] O. M. Hohn and A. Gülhan, "Experimental investigation of sidewall compression and internal contraction in a scramjet inlet," *J. Propuls. Power*, vol. 33, no. 2, pp. 501–513, Mar. 2017.

[14] G. M. Currao, A. J. Neely, D. R. Buttsworth, and S. L. Gai, "Hypersonic fluid-structure interaction on a cantilevered plate," in *Proc. 7th Eur. Conf. Aeronaut. Space Sci.*, vol. 12, 2017, pp. 1–14.

[15] P. B. Vasconcelos, L. McQuellin, K. Talluru, and A. Neely, "Hypersonic fluid-structure interactions on a compliant clamped-free-clamped-free panel under the influence of static shock impingement," in *Proc. AIAA SCITECH Forum*, 2022, p. 241.

[16] G. M. D. Currao, A. J. Neely, C. M. Kennell, S. L. Gai, and D. R. Buttsworth, "Hypersonic fluid–structure interaction on a cantilevered plate with shock impingement," *AIAA J.*, vol. 57, no. 11, pp. 4819–4834, Nov. 2019, doi: 10.2514/1.j058375.

[17] H. Babinsky and J. K. Harvey, *Shock Wave-Boundary-Layer Interactions*. Cambridge, U.K.: Cambridge Univ. Press, 2011.

[18] P. B. Vasconcelos, L. P. McQuellin, T. Krishna, and A. Neely, "Experimental study of hypersonic fluid-structure interactions on an inclined clamped-free-clamped-free compliant panel," in *Proc. ASCEND*, 2021, p. 4232, doi: 10.2514/6.2021-4232.

[19] S. Bhattrai, L. P. McQuellin, G. Currao, A. Neely, and D. R. Buttsworth, "Experimental study of the aeroelastic response and performance of a hypersonic intake," in *Proc. 23rd AIAA Int. Space Planes Hypersonic Syst. Technol. Conf.*, Mar. 2020, pp. 755–780, doi: 10.2514/6.2020-2449.

[20] S. Bhattrai, L. McQuellin, G. M. Currao, A. Neely, and D. Buttsworth, "Influence of hypersonic fluid-structure interaction on the control authority of a trailing-edge flap," in *Proc. 22nd AIAA Int. Space Planes Hypersonics Syst. Technol. Conf.*, Sep. 2018, p. 5265, doi: 10.2514/6.2018-5265.

[21] M. C. Neet and J. M. Austin, "Effects of surface compliance on shock boundary layer interaction in the Caltech Mach 4 ludwieg tube," in *Proc. AIAA Scitech Forum*, 2020, p. 816, doi: 10.2514/6.2020-0816.

[22] D. Daub, B. Esser, and A. Gülhan, "Experiments on high-temperature hypersonic fluid–structure interaction with plastic deformation," *AIAA J.*, vol. 58, no. 4, pp. 1423–1431, Apr. 2020, doi: 10.2514/1.j059150.

[23] H. T. Pham, Z. N. Gianikos, and V. Narayanaswamy, "Compression ramp induced shock-wave/turbulent boundary-layer interactions on a compliant material," *AIAA J.*, vol. 56, no. 7, pp. 2925–2929, Jul. 2018, doi: 10.2514/1.j056652.

[24] M. A. Eitner, Y.-J. Ahn, L. Vanstone, M. N. Musta, J. Sirohi, and N. Clemens, "Effect of shock-wave boundary layer interaction on vibratory response of compliant panel," in *Proc. AIAA Aviation Forum*, 2021, p. 2493, doi: 10.2514/6.2021-2493.

[25] T. J. Whalen, A. G. Schöneich, S. J. Laurence, B. T. Sullivan, D. J. Bodony, M. Freydin, E. H. Dowell, and G. M. Buck, "Hypersonic fluid–structure interactions in compression corner shock-wave/boundary-layer interaction," *AIAA J.*, vol. 58, no. 9, pp. 4090–4105, Sep. 2020, doi: 10.2514/1.j059152.

[26] K. R. Brouwer, R. Perez, T. J. Beberniss, S. M. Spottswood, and D. A. Ehrhardt, "Fluid-structure interaction on a thin panel including shock impingement effects," in *Proc. AIAA Scitech Forum*, 2021, p. 910, doi: 10.2514/6.2021-0910.

[27] S. M. Spottswood, T. J. Beberniss, T. G. Eason, R. A. Perez, J. M. Donbar, D. A. Ehrhardt, and Z. B. Riley, "Exploring the response of a thin, flexible panel to shock-turbulent boundary-layer interactions," *J. Sound Vibrat.*, vol. 443, pp. 74–89, Mar. 2019, doi: 10.1016/j.jsv.2018.11.035.

[28] L. Pollock, H. Kleine, A. Neely, and G. Wild, "Measuring fluid structure interaction in a cantilevered panel using optical fiber Bragg gratings," in *Proc. AIAA Aviation Forum*, Jun. 2023, p. 3605, doi: 10.2514/6.2023-3605.

[29] L. Pollock and G. Wild, "Modal analysis of a scramjet inlet for optimization of sensor placement," in *Proc. ASCEND*, Nov. 2021, doi: 10.2514/6.2021-4084.

[30] A. Bertholds and R. Dandliker, "Determination of the individual strain-optic coefficients in single-mode optical fibres," *J. Lightw. Technol.*, vol. 6, no. 1, pp. 17–20, Jan. 1988, doi: 10.1109/50.3956.

[31] P. Wang, G. Farrell, Q. Wang, and G. Rajan, "An optimized macrobending-fiber-based edge filter," *IEEE Photon. Technol. Lett.*, vol. 19, no. 15, pp. 1136–1138, Aug. 1, 2007, doi: 10.1109/LPT.2007.901434.

[32] G. S. Settles, *Schlieren and Shadowgraph Techniques: Visualizing Phenomena in Transparent Media*. Berlin, Germany: Springer, 2001.

[33] M. K. Vairalkar and S. Nimbhorkar, "Edge detection of images using Sobel operator," *Int. J. Emerg. Technol. Adv. Eng.*, vol. 2, no. 1, pp. 291–293, 2012.

[34] E. Aybar, "Sobel edge detection method for MATLAB," Anadolu Univ., Eskişehir, Türkiye, Tech. Rep. 26410, 2006.

[35] W. H. H. J. Lunscher and M. P. Beddoes, "Fast binary-image boundary extraction," *Comput. Vis., Graph., Image Process.*, vol. 38, no. 3, pp. 229–257, Jun. 1987, doi: 10.1016/0734-189x(87)90112-5.

[36] V. Sridhar, K. Hiraki, S. L. Gai, and H. Kleine, "Digital streak imaging of compressible flows," *Opt. Lasers Eng.*, vol. 160, Jan. 2023, Art. no. 107280.

[37] Z. Peng, F. Chu, and Y. He, "Vibration signal analysis and feature extraction based on reassigned wavelet scalogram," *J. Sound Vibrat.*, vol. 253, no. 5, pp. 1087–1100, Jun. 2002.

[38] F. Axisa and J. Antunes, *Modelling of Mechanical Systems: Fluid-Structure Interaction*. Amsterdam, The Netherlands: Elsevier, 2006.

[39] H. L. Ho, W. Jin, C. C. Chan, Y. Zhou, and X. W. Wang, "A fiber Bragg grating sensor for static and dynamic measurands," *Sens. Actuators A, Phys.*, vol. 96, no. 1, pp. 21–24, Jan. 2002, doi: 10.1016/s0924-4247(01)00762-2.

[40] J. D. Anderson, *Hypersonic and High Temperature Gas Dynamics*, 2000, doi: 10.2514/4.105142.

[41] T. Li, Y. Tan, Z. Zhou, and K. Zheng, "A non-contact FBG vibration sensor with double differential temperature compensation," *Opt. Rev.*, vol. 23, no. 1, pp. 26–32, Feb. 2016, doi: 10.1007/s10043-015-0153-y.

[42] Y. Xiao, Y. Wang, J. Shi, D. Zhu, and Q. Liu, "Temperature-insensitive and sensitivity-enhanced FBG strain sensor by using parallel MPF," *IEEE Photon. Technol. Lett.*, vol. 35, no. 15, pp. 809–812, Aug. 1, 2023, doi: 10.1109/lpt.2023.3281472.

[43] Y. Liu, Y. Feng, J. Wen, L. Huang, and J. Dong, "Integrated fiber-optic sensor based on inscription of FBG in seven-core fiber for curvature and temperature measurements," *Opt. Fiber Technol.*, vol. 75, Jan. 2023, Art. no. 103197, doi: 10.1016/j.yofte.2022.103197.

[44] T. Guo, X. Qiao, Z. Jia, Q. Zhao, and X. Dong, "Simultaneous measurement of temperature and pressure by a single fiber Bragg grating with a broadened reflection spectrum," *Appl. Opt.*, vol. 45, no. 13, p. 2935, 2006, doi: 10.1364/ao.45.002935.

[45] C. Caucheteur, F. Lhommé, K. Chah, M. Blondel, and P. Mégret, "Simultaneous strain and temperature sensor based on the numerical reconstruction of polarization maintaining fiber Bragg gratings," *Opt. Lasers Eng.*, vol. 44, no. 5, pp. 411–422, May 2006, doi: 10.1016/j.optlaseng.2005.06.002.

[46] Y. Jiang, C. Liu, D. Li, D. Yang, and J. Zhao, "Simultaneous measurement of temperature and strain using a phase-shifted fiber Bragg grating inscribed by femtosecond laser," *Meas. Sci. Technol.*, vol. 29, no. 4, Apr. 2018, Art. no. 045101, doi: 10.1088/1361-6501/aa9f6a.

[47] T. Yamaguchi, W. Endo, and Y. Shinoda, "Interrogation system with automatic recognition and delay correction functions of fiber Bragg gratings by pulse modulation with wavelength-swept laser," *IEEE Sensors J.*, vol. 19, no. 22, pp. 10519–10528, Nov. 2019, doi: 10.1109/JSEN.2019.2933812. https://doi.org/10.1109/JSEN.2019.2933812

LUKE POLLOCK was born in Melbourne, Australia. He received the B.Eng. degree (Hons.) in aerospace engineering from the Royal Melbourne institute of Technology (RMIT), Melbourne, Australia in, 2020. He is currently pursuing the Ph.D. degree with the University of New South Wales Canberra (UNSW Canberra), Campbell, Australia, with a focus on structural health monitoring and non-destructive testing technologies for high-speed vehicles.

Since 2022, he has been a Research Associate with UNSW Canberra, studying aerothermal shape distortion of hypersonic vehicles.

Mr. Pollock is currently a member of Engineers Australia (EA), American Institute of Aeronautics and Astronautics (AIAA), Australian Division, Royal Aeroanutical Society (RAeS), and the University Consortium of Applied Hypersonics (UCAH), and an Associate Fellow of the Higher Education Academy (HEA). He was awarded the Best Presentation from the 12th DST International Conference on Health and Usage Monitoring.

HARALD KLEINE was born in Krefeld, Germany. He received the Dipl.-Ing. and Dr.-Ing. degrees from RWTH Aachen University.

After a postdoctoral fellowship at McGill University, Montreal, Canada, and a two-year appointment as a Research Engineer for Med-Eng Systems, Ottawa, Canada, he joined Tohoku University, Sendai, Japan, for three years. In 2002, he joined the University of New South Wales Canberra, where he is currently an Associate Professor. He has been the author or co-author of more than 160 publications (book chapters, journal articles and conference contributions). As many compressible flow problems are highly transient, an important focus of his work has been the application of high-speed camera systems. His main interests include developing and applying methods to visualize compressible flows, which typically leads to extensions and customizations of density-sensitive visualization methods.

ANDREW NEELY received the bachelor's degree in mechanical engineering, the master's degree in engineering science, and the Ph.D. degree in hypersonics from The University of Queensland.

After graduating the Ph.D. degree, he spent almost eight years with the Osney Thermofluids Laboratory, University of Oxford, Rolls-Royce-funded working on industrial jet engine projects as well as teaching. He returned to Australia to take up a faculty position at the University of New South Wales Canberra (UNSW Canberra) where is currently a Professor of aerospace engineering and the Associate Dean of Research Engagement. At UNSW Canberra, he leads a research group developing experimental and numerical techniques to predict and improve the design and performance of high-speed flight vehicles and propulsion systems and collaborates with a wide range of international partners including on a number of flight-test projects. He has published more than 200 technical papers.

Dr. Neely is the Australian Board Member of the International Society for Air Breathing Engines (ISABE). He has served on international technical and management committees for the Royal Aeronautical Society (RAeS), American Institute of Aeronautics and Astronautics (AIAA), the Institute of Mechanical Engineers (IMechE), and American Society of Mechanical Engineers (ASME). From 2017 to 2019, he was the Vice President of ISABE and the President of Australian Division, RAeS.

GRAHAM WILD (Member, IEEE) was born in Rotherham, U.K., in 1981. He received the B.Sc. degree in physics and mathematics and the B.Sc. (Hons.) degree in physics from Edith Cowan University, Joondalup, WA, Australia, in 2004 and 2005, respectively, the M.Sc. (Tech.) degree in photonics and optoelectronics from the University of New South Wales, Sydney, Australia, in 2008, and the Ph.D. degree in engineering from Edith Cowan University, in 2010. He received the Graduate Certificate in research commercialization from Queensland University of Technology, Brisbane, QLD, Australia, in 2008

He has completed two research internships with the Australian CSIRO Industrial and Telecommunications Physics Division, from 2003 to 2004 (with the Electric Machines Group), and from 2004 to 2005 (with the Intelligent Systems Group), Sydney, Australia. In 2010, he was a Postdoctoral Research Fellow with the Optical Research Laboratory, Edith Cowan University. From 2011 to 2012, he was a Lecturer in Aircraft Systems with Edith Cowan University. From 2012 to 2019, he was a Senior Lecturer in aerospace engineering and aviation with RMIT University, Melbourne, Australia. Since 2020, he has been a Senior Lecturer in aviation technology with the University of New South Wales Canberra (UNSW Canberra), Australia. He has authored and co-authored more than 150 scientific papers. His current research interests include intelligent systems, AI, data and analytics, and advanced technology in aviation and aerospace, for safety and sustainability.

Dr. Wild is a member of SPIE and RAeS.